Computers and Mathematics with Applications 66 (2013) 304–317

Contents lists available at SciVerse ScienceDirect

Computers and Mathematics with Applications

journal homepage: www.elsevier.com/locate/camwa

Evaluation of weakly compressible SPH variants using derived analytical solutions of Taylor–Couette flows

Pablo S. Rojas Fredini *,[1], Alejandro C. Limache [2]

International Center of Computational Methods in Engineering (CIMEC), INTEC-CONICET, Güemes 3450, Santa Fe (3000), Argentina

ARTICLE INFO

Article history:
Received 28 August 2012
Received in revised form 7 February 2013
Accepted 19 May 2013

Keywords:
Smoothed particle hydrodynamics
Navier–Stokes equations
Taylor–Couette flows
Analytical solutions
Pseudo-incompressible flows

ABSTRACT

Smoothed particle hydrodynamics (SPH) is a relatively young meshless particle method used in fluid simulation. The method has not yet reached a mature state and still is in the need of rigorous evaluation tests that contribute to its consolidation as a reliable numerical method. With this need in mind, the first portion of this article is dedicated to presenting a new set of validation tests. The tests consist of different types of planar Taylor–Couette flows which will be equipped with their corresponding Navier–Stokes equations' analytical solutions. Analytical solutions have been found for compressible and weakly-compressible (WC) regimes. The second part of this article is dedicated to using the obtained solutions as evaluation tests of a WC-SPH variant based on the divergence form of the Navier–Stokes equations and on the simultaneous use of different kernels. The proposed variant is compared to other previous WC-SPH variants commonly used in the literature. Velocities as well as pressure profiles can be compared with the provided analytical solutions. The performed numerical experiments show that, although all the tested WC-SPH variants match quite correctly the theoretical velocity profile, the previous variants present highly noisy pressure profiles or even give erroneous pressure solutions. Among the evaluated WC-SPH formulations, the proposed variant does a better job in matching, both, velocity profiles and pressure profiles with much lower levels of noise.

1. Introduction

Smoothed particle hydrodynamics (SPH) is a meshless particle method which was first invented to simulate astrophysical phenomena [1,2] and many works have followed [3–8]. More recently, SPH has been successfully applied in the simulation of solids and fluids. Including simulation of fluid–structure interaction [9–11] and discontinuous fields [12]. In these areas, SPH competes against other particle methods like the Particle Finite Element Method (PFEM) [13,14]. SPH is also currently used to add realistic physical behavior to interactive applications like videogames, surgery simulators and virtual reality environments [15–17]. Detailed reviews of the method and its different applications can be found in [12,18].

In the fluid mechanics context, different SPH variants of the original method have been proposed. The variants differ in how the boundary conditions are imposed, or in the different smoothing kernels used, or in the different discrete expressions of the gradient and other differential operators used. Regarding boundary conditions mainly two formulations have been used to simulate walls and other boundaries. One type makes use of mirrored ghost particles [19–21] and the second one uses

* Corresponding author. Tel.: +54 03434241517.
E-mail addresses: srojasfredini@live.com.ar, srojasfredini@santafe-conicet.gov.ar (P.S. Rojas Fredini), alejandrolimache@gmail.com (A.C. Limache).
URL: http://www.cimec.org.ar/PMgroup (A.C. Limache).
1 Doctoral fellow.
2 CONICET Researcher.

0898-1221/$ – see front matter © 2013 Elsevier Ltd. All rights reserved.
http://dx.doi.org/10.1016/j.camwa.2013.05.008

additional particles positioned on the wall, simulating the real solid boundary [22,23]. Special care must be taken when using the second approach due to the particle deficiency on the boundary [12]. Also combinations of both approaches have been suggested [12]. Different smoothing kernels have been proposed [24,12,25]. Also different SPH variants have been proposed for dealing with the gradient, the divergence and the Laplacian operators [12,18,26–28]. Finally, regarding the simulation of incompressible fluids, two approaches are used nowadays. One approach forces incompressibility in strong form leading to variants named I-SPH [29–32] while the other approach forces incompressibility weakly by simulating a weakly-compressible (WC) fluid leading to variants named WC-SPH [33–35]. The I-SPH approach leads to implicit formulations requiring the solution of a system of equations while WC-SPH leads to fully-explicit formulations not requiring the solution of any system of equations. This property makes WC-SPH variants easier to implement in parallel computation.

Significant improvements to the original SPH method have been obtained since the method was born, but there is still a lot to be investigated about the method and its behavior. Like any other numerical method, the mathematical background must be strengthened and more exhaustive validations must be made in order to consolidate it. Following this need, in this research focus has been made on verifying and testing a group of WC-SPH variants through a series of numerical flow simulations. The proposed tests consist of the simulation of planar Taylor–Couette flows (i.e. flows between coaxial cylinders) like the one depicted in Fig. 1 where A and B are the inner and outer cylinder walls respectively. These flows form a series of benchmark tests because they can be equipped with the corresponding analytical solutions of the Navier–Stokes equations. The analytical solution for the incompressible regime is well known and extensively described in fluid textbooks. For compressible fluids (including weakly-compressible fluids) the solution will be derived and presented in the first part of the paper. Next the obtained solutions will be used as evaluation tests of a proposed WC-SPH variant. The proposed formulation is based on the divergence form of the Navier–Stokes equations and on the simultaneous use of different kernels. Finally, numerical tests are performed so as to compare the new variant with previous WC-SPH variants reported in the literature.

2. Navier–Stokes equations

2.1. Differential forms of the Navier–Stokes equations

Next, the Eulerian and Lagrangian form of the Navier–Stokes equations will be presented. The Eulerian description will be used to derive the analytical solutions of the flow equations while the Lagrangian description will be used by the SPH formulations.

2.1.1. Eulerian description

The equation of mass conservation given in Eulerian description is given by

$$\frac{\partial \rho}{\partial t} + \nabla \cdot (\rho \boldsymbol{v}) = 0 \tag{1}$$

while the momentum equations can be expressed in Divergence Form as

$$\rho \frac{\partial \boldsymbol{v}}{\partial t} + \rho(\nabla \boldsymbol{v}) \cdot \boldsymbol{v} = -\nabla p + \nabla \cdot \boldsymbol{\tau} \tag{2}$$

or in Laplace Form as

$$\rho \frac{\partial \boldsymbol{v}}{\partial t} + \rho \nabla \boldsymbol{v} \cdot \boldsymbol{v} = -\nabla p + \mu \nabla^2 \boldsymbol{v} + \frac{\mu}{3} \nabla(\nabla \cdot \boldsymbol{v}). \tag{3}$$

In the above equations, ρ, $\boldsymbol{v}$, p and $\boldsymbol{\tau}$, are the density, velocity, pressure and the viscous stress tensor of the fluid, respectively. As the fluid is Newtonian $\boldsymbol{\tau}$ is computed as

$$\boldsymbol{\tau} = \mu \left[\nabla \boldsymbol{v} + \nabla \boldsymbol{v}^T \right] - \frac{2}{3} \mu (\nabla \cdot \boldsymbol{v}) \boldsymbol{I} \tag{4}$$

where $\boldsymbol{I}$ is the Identity tensor.

2.1.2. Lagrangian description

Alternatively, the Navier–Stokes equations can be written in a Lagrangian description by replacing local (Eulerian) time-derivatives $\frac{\partial}{\partial t}$ in terms of material (Lagrangian) time-derivatives $\frac{D}{Dt}$. In the Lagrangian description, the equation of conservation of mass (Eq. (1)) is given by

$$\frac{D\rho}{Dt} + \rho \nabla \cdot \boldsymbol{v} = 0 \tag{5}$$

and the momentum equations can be expressed in Divergence Form as

$$\rho \frac{D\boldsymbol{v}}{Dt} = -\nabla p + \nabla \cdot \boldsymbol{\tau} \tag{6}$$

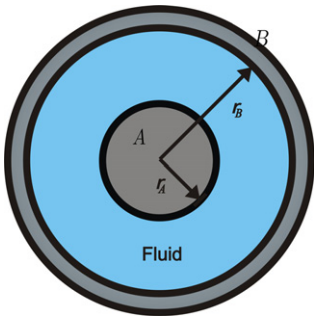

Fig. 1. Planar Taylor–Couette flow or annular cavity flow.

or in Laplace Form as:

$$\rho\frac{D\boldsymbol{v}}{Dt} = -\nabla p + \mu\nabla^2\boldsymbol{v} + \mu\frac{1}{3}\nabla(\nabla\cdot\boldsymbol{v}). \tag{7}$$

2.2. Equation of state

For compressible and weakly-compressible flows, the pressure and density are linked through the equation of state. Here it will be assumed that the equation of state has the general form used in WC-SPH formulations:

$$p = \kappa\left(\left(\frac{\rho}{\rho_0}\right)^{\gamma} - 1\right). \tag{8}$$

In terms of the speed of sound c_s, κ is given by

$$\kappa = \frac{\rho_0 c_s^2}{\gamma}. \tag{9}$$

Note that the inverse of Eq. (8) is:

$$\rho = \rho_0\left(\frac{p}{\kappa} + 1\right)^{1/\gamma}. \tag{10}$$

3. Analytical solutions of Navier–Stokes equations for steady planar Taylor–Couette flows

3.1. Planar Taylor–Couette flows or annular cavity flows

When the flow is planar (i.e. there is no velocity in the axial direction), the problem can be thought of as a two dimensional flow in an annular cavity as depicted in Fig. 1. The inner cylinder A and the external cylinder B can have arbitrary radius, r_A and r_B, respectively, and they can rotate independently with different angular velocities, ω_A and ω_B, respectively. The cylindrical walls can be assumed to be either of the slip type or the non-slip type. As a consequence, different types of steady flows, can be obtained for different values of the design parameters $\{r_A, r_B, \omega_A, \omega_B$, slip condition$\}$, as shown schematically in Fig. 2.

3.2. General analytical solutions

A general set of analytical solutions for the velocity and pressure can be obtained for steady flows in the annular cavity. Analytical solutions for the general case of compressible/pseudo-incompressible flows, satisfying the equation of state (8) commonly used in SPH, will be presented and derived.

To this end, consider the Eulerian description of the compressible Navier–Stokes equations (i.e. Eqs. (1) and (3)). For steady flows, they reduce to

$$\nabla\cdot(\rho\boldsymbol{v}) = \nabla\rho\cdot\boldsymbol{v} + \rho\nabla\cdot\boldsymbol{v} = 0 \tag{11}$$

$$\rho\nabla\boldsymbol{v}\cdot\boldsymbol{v} = -\nabla p + \mu\nabla^2\boldsymbol{v} + \frac{\mu}{3}\nabla(\nabla\cdot\boldsymbol{v}). \tag{12}$$

Using polar coordinates (r, θ) and assuming a planar flow ($v_z = 0$), the velocity vector can be written as:

$$\boldsymbol{v} = v_r\boldsymbol{e}_r + v_\theta\boldsymbol{e}_\theta. \tag{13}$$

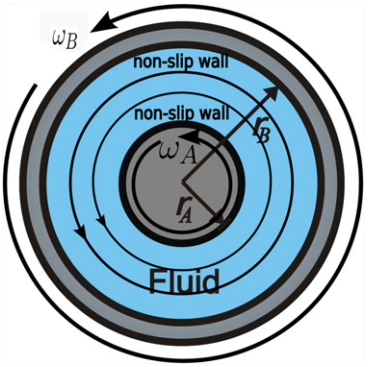

Fig. 2. Annular cavity steady flows for general design parameters $\{r_A, r_B, \omega_A, \omega_B\}$ with non-slip walls.

By symmetry, in an steady flow, it can be assumed that any physical field should not depend on θ and the streamlines should be circular, i.e:

$$v_r = v_r(r) = 0; \qquad v_\theta = v_\theta(r); \qquad \rho = \rho(r); \qquad p = p(r). \tag{14}$$

As a consequence $\nabla\rho \cdot \boldsymbol{v} = 0$, so the continuity equation (11) is satisfied identically. Note that for this case also holds $\nabla \cdot \boldsymbol{v} = \frac{1}{r}\frac{\partial(rv_r)}{\partial r} + \frac{1}{r}\frac{\partial(v_\theta)}{\partial\theta} = 0$.

The momentum equations reduce to:

$$\rho\nabla\boldsymbol{v} \cdot \boldsymbol{v} = -\nabla p + \mu\nabla^2\boldsymbol{v}. \tag{15}$$

Writing the Gradient and Laplace operators in polar coordinates and making use of steady-symmetry conditions (14), it can be shown that the (r, θ) momentum equations (15) reduce to the following differential equations:

$$-\frac{\rho}{r}v_\theta^2 = -\frac{\partial p}{\partial r} \tag{16}$$

$$0 = \left[\frac{\partial^2 v_\theta}{\partial r^2} + \frac{1}{r}\frac{\partial v_\theta}{\partial r} - \frac{v_\theta}{r^2}\right]. \tag{17}$$

Integration of the last equation, leads to the general analytical form of the velocity field:

$$v_r = 0; \qquad v_\theta = \frac{a}{r} + br. \tag{18}$$

Using the equation of state (10) and Eq. (18), the r-momentum equation becomes:

$$\frac{1}{r}\left[\frac{a}{r} + br\right]^2 = \frac{1}{\rho_0\left(\frac{p}{\kappa} + 1\right)^{1/\gamma}}\frac{\partial p}{\partial r}. \tag{19}$$

Assuming $\gamma \neq 1$, integration of both sides of the above equation from the inner-wall radius r_A to an arbitrary radius r, leads to the following general expression for the pressure in the annular cavity:

$$p = \kappa\left[\frac{\Gamma\rho_0}{\kappa}\Psi(r) + \left(\frac{p_A}{\kappa} + 1\right)^\Gamma\right]^{\frac{1}{\Gamma}} - \kappa \tag{20}$$

where

$$\Psi(r) = \frac{1}{2}\left[-a^2\left(\frac{1}{r^2} - \frac{1}{r_A^2}\right) + 4ab\ln(r/r_A) + b^2\left(r^2 - r_A^2\right)\right] \tag{21}$$

and $\Gamma = \frac{\gamma-1}{\gamma}$. For $\gamma = 1$ one gets that:

$$p = \kappa e^{\left[\frac{\rho_0}{\kappa}\Psi(r) + \ln\left(\frac{p_A}{\kappa}+1\right)\right]} - \kappa. \tag{22}$$

Note that while Eqs. (20)–(22) define the pressure profile for compressible fluids (and weakly-compressible fluids), the equivalent pressure profile for an incompressible fluid is simply given by:

$$p = \rho_0\Psi(r) + p_A. \tag{23}$$

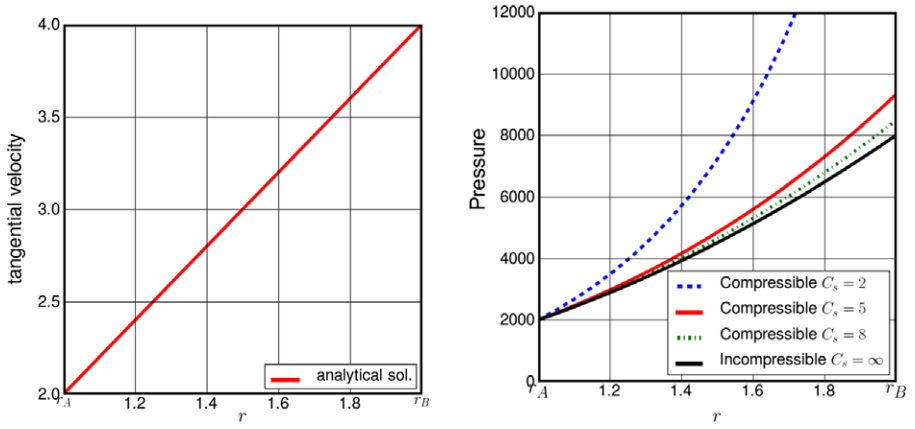

(a) Analytical velocity profile. (b) Analytical pressure profiles.

Fig. 3. Analytical velocity profile and pressure profiles for the case of co-rotating cylinders with $\omega_A = \omega_B = \omega = 2$ with different fluid's compressibility levels.

The incompressible solution can be obtained by re-integrating the r-momentum equation (16) with a constant density ρ_0 (see Ref. [36] for more details).

3.3. Analytical solutions for non-slip walls

With the general solutions at hand, one can get specific solutions by imposing different boundary conditions to the cylindrical walls. For solid non-slip walls, the following boundary conditions must hold:

$$v_\theta(r_A) = V_A = \omega_A r_A; \qquad v_\theta(r_B) = V_B = \omega_B r_B. \tag{24}$$

Using Eqs. (24) into Eq. (18), it can be shown that the general solution for non-slip walls is:

$$v_r = 0; \qquad v_\theta = \frac{a}{r} + br \tag{25}$$

where

$$a = -\frac{r_B^2 r_A^2}{(r_B^2 - r_A^2)}(\omega_B - \omega_A); \qquad b = \frac{\omega_B r_B^2 - \omega_A r_A^2}{(r_B^2 - r_A^2)}. \tag{26}$$

Observation 1: Note from Eqs. (25) and (26) that the velocity profile is independent of the compressibility (κ, γ) of the fluid and also independent of the fluid viscosity μ. On the other hand, from Eqs. (20), (21) and (26) it follows that the pressure profile depends on fluid's compressibility but, like the velocity, it is independent of the fluid's viscosity.

3.3.1. Co-rotating cylinders

When both cylinders rotate with the same angular velocity $\omega_B = \omega_A = \omega$, Eqs. (25) and Eqs. (20)–(22) give the following flow solution:

$$v_r = 0; \qquad v_\theta = \omega r \tag{27}$$

$$p = \begin{cases} \kappa\left[\dfrac{\Gamma\rho_0}{\kappa}\dfrac{\omega^2}{2}\left(r^2 - r_A^2\right) + \left(\dfrac{p_A}{\kappa} + 1\right)^{\Gamma}\right]^{\frac{1}{\Gamma}} - \kappa & \text{for } \gamma \neq 1 \\ \kappa e^{\left[\frac{\rho_0}{\kappa}\frac{\omega^2}{2}\left(r^2 - r_A^2\right) + \ln\left(\frac{p_A}{\kappa}+1\right)\right]} - \kappa & \text{for } \gamma = 1. \end{cases} \tag{28}$$

Then, in the case of co-rotating cylinders, the tangential flow velocity v_θ varies linearly with r, and the steady flow acquires a rigid-like motion, rotating together with the walls at the same angular velocity ω. Fig. 3(a) and (b) show plots of the analytical velocity and pressure profiles (27) and (28), respectively, for fluids with different levels of compressibility. The different parameters chosen for the annular cavity are: $r_A = 1$, $r_B = 2$, $\omega_A = \omega_B = \omega = 2$. All plotted fluids have a value of γ equal to 1, with compressibility values: $c_s = 2$, $c_s = 5$, $c_s = 8$ (for each fluid κ is computed from Eq. (9)). In Fig. 3(b), for comparison purposes, the pressure profile corresponding to the incompressible case is also shown. Notably, there is a small pressure difference between the compressible case with $c_s = 8$ and the incompressible case. This indicates that by augmenting the speed of sound c_s, compressible fluids can behave practically like an incompressible fluid to any degree of accuracy.

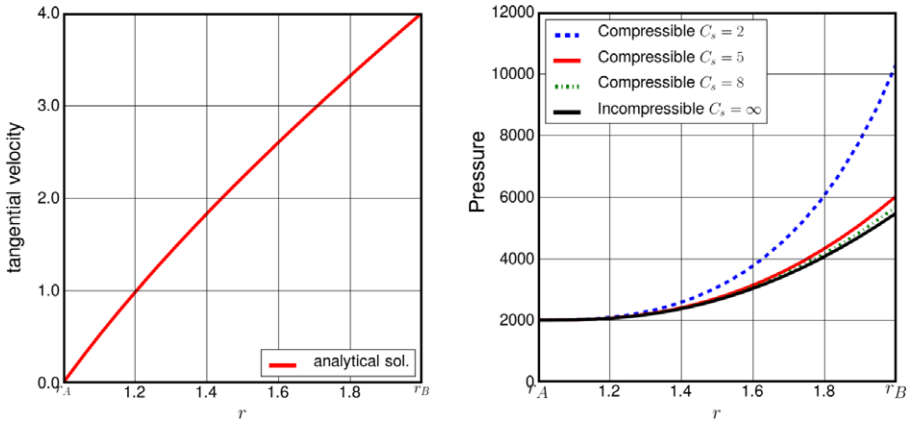

(a) Analytical velocity profile. (b) Analytical pressure profiles.

Fig. 4. Analytical velocity profile and pressure profiles for the case of a fixed inner cylinder $\omega_A = 0$ and a rotating external cylinder $\omega_B = 2$ with different fluid's compressibility levels.

3.3.2. Rotating outer cylinder, fixed inner cylinder

If cylinder A is kept fixed ($\omega_A = 0$) while B rotates, the tangential velocity is given by

$$v_\theta = -\frac{\omega_B r_B^2 r_A^2}{(r_B^2 - r_A^2)}\frac{1}{r} + \frac{\omega_B r_B^2}{(r_B^2 - r_A^2)} r. \tag{29}$$

Note that in this case, the flow not longer moves in a rigid-like motion with the velocity profile not longer being linear. Fig. 4(a) and (b) show plots of the analytical velocity and pressure profiles, respectively, associated to the three compressible fluids defined previously ($\gamma = 1$, with $c_s = 2$, $c_s = 5$ and $c_s = 8$). The chosen values of the annular cavity parameters are: $r_A = 1, r_B = 2, \omega_A = 0, \omega_B = 2$. In Fig. 4(b), for comparison purposes, the pressure profile corresponding to the incompressible case is also shown. Note again the small difference between the compressible and the incompressible pressure solutions as c_s is increased.

Next, in Section 4, the key concepts of the SPH method will be presented. In Section 5, our proposed WC-SPH variant together with other WCSPH variants previously mentioned in the literature will be introduced. Finally, in Section 6, the numerical solutions obtained with these WC-SPH variants will be compared against the analytical solutions obtained in this section.

4. SPH key concepts

4.1. Smoothing kernel and function approximation

SPH is a particle method based on the integral approximation $\langle f(\boldsymbol{r})\rangle$ around a point $\boldsymbol{r}$ in space of an arbitrary field function $f(\boldsymbol{r}')$ in terms of the convolution of the function values with a smoothing kernel function W:

$$\langle f(\boldsymbol{r})\rangle = \int_V f(\boldsymbol{r}')W(\boldsymbol{r} - \boldsymbol{r}', h)dV'. \tag{30}$$

The integral approximation $\langle f_i\rangle$ of f at each particle i is computed numerically by adding the elemental contributions of the surrounding j-particles located inside the support domain $|\boldsymbol{r}_i - \boldsymbol{r}_j| \leq h$ of the kernel function.

$$\langle f_i\rangle = \langle f(\boldsymbol{r}_i)\rangle = \sum_{j=1}^{n} \frac{m_j}{\rho_j} f_j W_{ij} \tag{31}$$

where in the equation above m_j, ρ_j and f_j are the mass, density and values of f in each neighbor particle j, respectively. Also, W_{ij} denotes $W(\boldsymbol{r}_i - \boldsymbol{r}_j, h)$.

4.2. Gradient approximations

Similarly (see [12]), the gradient ∇f of a function f at particle i can be approximated by the following expression:

$$\langle \nabla f_i\rangle = \langle \nabla f(\boldsymbol{r}_i)\rangle = \sum_j m_j \frac{f_j}{\rho_j} \nabla_i W_{ij} \tag{32}$$

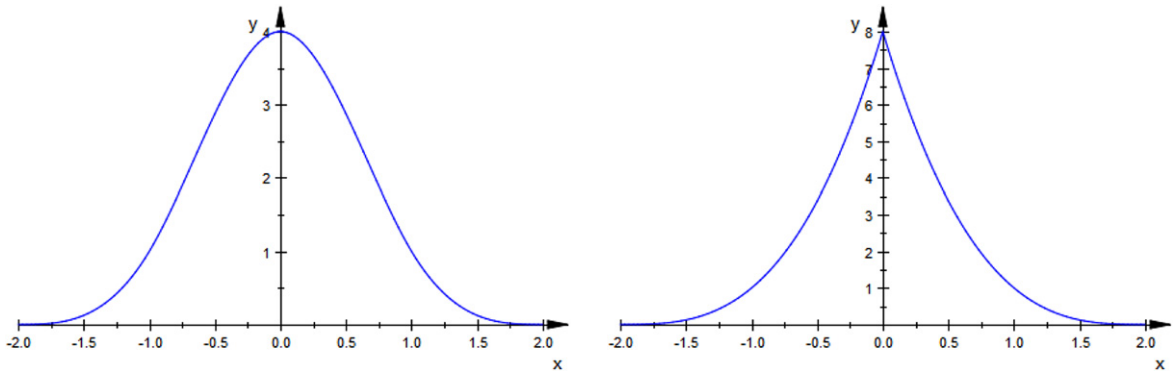

(a) Cubic spline. (b) Spiky.

Fig. 5. SPH Kernels used in the verification.

where in the above expression ∇_i denotes the gradient taken with respect to the coordinates of particle i. In SPH, other particle approximations can be derived for computing gradients [12,37]:

$$\langle \nabla f_i \rangle = \sum_j m_j \frac{f_j - f_i}{\rho_j} \nabla_i W_{ij} \tag{33}$$

$$\langle \nabla f_i \rangle = \sum_j m_j \frac{f_j - f_i}{\rho_i} \nabla_i W_{ij} \tag{34}$$

$$\langle \nabla f_i \rangle = \sum_j m_j \frac{f_j + f_i}{\rho_j} \nabla_i W_{ij} \tag{35}$$

$$\langle \nabla f_i \rangle = \rho_i \sum_j m_j \left(\frac{f_i}{\rho_i^2} + \frac{f_j}{\rho_j^2} \right) \nabla_i W_{ij}. \tag{36}$$

Muller et al. [15] has also proposed:

$$\langle \nabla f_i \rangle = \sum_j m_j \frac{f_j + f_i}{2\rho_j} \nabla_i W_{ij}. \tag{37}$$

4.3. Kernel functions

There exist several possible kernel functions. Here, only two of the most commonly used kernel functions are considered. The first one is the cubic spline [38,5] which is given by the following expression:

$$W(\boldsymbol{r}, h) = K_d \begin{cases} (2-q)^3 - 4(1-q)^3, & \text{for } 0 \leqslant q \leqslant 1 \\ (2-q)^3, & \text{for } 1 \leqslant q \leqslant 2 \\ 0, & \text{for } 2 < q \end{cases} \tag{38}$$

where q is defined as $\frac{2r}{h}$ and where r is the Euclidean distance $r = |\boldsymbol{r}|$. In 2-dimensional space, the normalization constant is equal to $K_d = \frac{10}{7\pi h^2}$. The other selected kernel is the Spiky Kernel [25] which is given by

$$W(\boldsymbol{r}, h) = K_d \begin{cases} (2-q)^3 & \text{for } 0 \leqslant q \leqslant 2 \\ 0, & \text{for } 2 < q. \end{cases} \tag{39}$$

In 2-dimensional space the normalization constant is equal to $K_d = \frac{5}{4\pi h^2}$. In Fig. 5 both kernels can be seen.

5. WC-SPH formulations

5.1. Particle approximations of density

In WC-SPH, the fluid density in the particles can be determined by applying the fundamental SPH particle approximation given in Eq. (31) to the density itself:

$$\rho_i = \sum_j m_j W_{ij}. \tag{40}$$

Other WC-SPH formulations compute the density by time-integration of the discrete equation that results from application of the SPH particle approximation to the equation of conservation of mass (5). For example using the particle approximation (33) for computing the divergence term, one gets:

$$\frac{D\rho_i}{Dt} = -\rho_i \sum_j m_j \frac{\boldsymbol{v}_j - \boldsymbol{v}_i}{\rho_j} \cdot \nabla_i W_{ij}. \tag{41}$$

Other similar expressions can be found in Table 4.1 of Ref. [12].

5.2. Particle approximations of momentum equations

In SPH, the fluid velocities in the particles are determined by time-integration of the discrete accelerations that result from application of an SPH particle approximation to the equations of conservation of momentum defined in Eq. (6):

$$\frac{D\boldsymbol{v}_i}{Dt} = \frac{1}{\rho_i}\langle \nabla p_i \rangle + \frac{1}{\rho_i}\langle \nabla \cdot \boldsymbol{\tau}_i \rangle. \tag{42}$$

We can write the above equation in compact form as:

$$m_i \frac{D\boldsymbol{v}_i}{Dt} = \boldsymbol{F}_i^{\text{press}} + \boldsymbol{F}_i^{\text{visc}} + \boldsymbol{F}_i^{\text{av}} \tag{43}$$

where:

$$\boldsymbol{F}_i^{\text{press}} = \frac{m_i}{\rho_i}\langle \nabla p_i \rangle \tag{44}$$

and

$$\boldsymbol{F}_i^{\text{visc}} = \frac{m_i}{\rho_i}\langle \nabla \cdot \boldsymbol{\tau}_i \rangle \tag{45}$$

and where in (43) an additional artificial-viscosity stabilizing force $\boldsymbol{F}^{\text{av}}$ has been added that will be defined in Section 5.3.

In our proposed variant, $\boldsymbol{F}_i^{\text{press}}$ and $\boldsymbol{F}_i^{\text{visc}}$ are computed using the symmetric gradient approximation defined in Eq. (35), that is to say:

$$\boldsymbol{F}_i^{\text{press}} = \frac{m_i}{\rho_i}\langle \nabla p_i \rangle = \sum_j m_i m_j \left(\frac{p_j + p_i}{\rho_i \rho_j} \right) \nabla_i W_{ij} \tag{46}$$

and

$$\boldsymbol{F}_i^{\text{visc}} = \frac{m_i}{\rho_i}\langle \nabla \cdot \boldsymbol{\tau}_i \rangle = \sum_j m_i m_j \left(\frac{\boldsymbol{\tau}_j + \boldsymbol{\tau}_i}{\rho_i \rho_j} \right) \cdot \nabla_i W_{ij}. \tag{47}$$

We have chosen the symmetric forms (46)–(47) because among the possible variants that can be obtained from Eqs. (32)–(37), it is the one that seems to give the best results. Other tested possible forms, give either poorer or the same results. It is worth mentioning that the alternative pressure approximation used in several works [39,15,40] and obtained from Eq. (37), i.e.:

$$\boldsymbol{F}_i^{\text{press}} = \frac{m_i}{\rho_i}\langle \nabla p_i \rangle = \sum_j m_i m_j \left(\frac{p_j + p_i}{2\rho_i \rho_j} \right) \nabla_i W_{ij} \tag{48}$$

gives a completely erroneous pressure profile. This will be seen in Section 6. In Table 4.1 of Ref. [12] and in Refs. [28,26,27,3] other possible formulas that could be tested are presented. In our formulation, the values of the tensor stress $\boldsymbol{\tau}_i$ at each particle i are computed by using Eq. (4), once the velocity gradient $\nabla \boldsymbol{v}$ is computed using the particle approximation (33):

$$\nabla \boldsymbol{v}_i = \langle \nabla \boldsymbol{v}_i \rangle = \sum_j m_j \left(\frac{\boldsymbol{v}_j - \boldsymbol{v}_i}{\rho_j} \right) \nabla_i W_{ij}. \tag{49}$$

5.3. Artificial viscosity

In SPH it is a standard procedure to add an artificial viscosity term to the velocity SPH momentum equations. Following the works of Clearly [27] and Monaghan [18], this term has the following general form:

$$\boldsymbol{F}_i^{\text{av}} = -\sum_j m_i m_j \Pi_{ij} \nabla_i W_{ij} \tag{50}$$

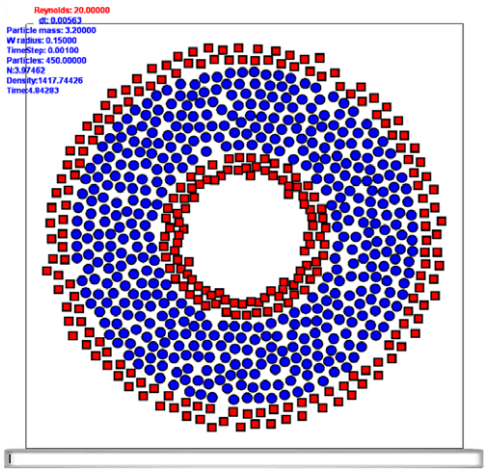

Fig. 6. Typical distribution of real particles and corresponding ghost particles. (For interpretation of the references to colour in this figure legend, the reader is referred to the web version of this article.)

with Π_{ij} given by

$$\Pi_{ij} = -\nu \left(\frac{\boldsymbol{v}_{ij} \cdot \boldsymbol{r}_{ij}}{|\boldsymbol{r}_{ij}|^2 + \eta^2} \right) \tag{51}$$

where

$$\nu = \frac{\bar{h}_{ij}}{\bar{\rho}_{ij}} \left(\alpha c_s - \beta \frac{\bar{h}_{ij} \boldsymbol{v}_{ij} \cdot \boldsymbol{r}_{ij}}{|\boldsymbol{r}_{ij}|^2 + \eta^2} \right) \tag{52}$$

and where $\boldsymbol{v}_{ij} = \boldsymbol{v}_i - \boldsymbol{v}_j$ and $\boldsymbol{r}_{ij} = \boldsymbol{r}_i - \boldsymbol{r}_j$ while the quantities with overbar denote mean values.

5.4. Boundary conditions

The method that we have adopted in order to simulate solid walls is based on the use of ghost particles [41]. These ghost particles are located outside the boundary domain in the same way ghost charges are located in the *images method* of electrostatics. So for each real fluid particle "a" located at a short distance d_a from the solid boundary, a ghost$_a$ particle is created which is located at a distance d_a inside the wall. Fig. 6 shows the distribution of ghost particles for a typical flow simulation around the annular cavity, the real particles are represented by the blue circles while the active ghost particles are shown by the red squares. The same density ρ_a is assigned to the ghost particle:

$$\rho_{\text{ghost}} = \rho_a$$

while its velocity $\boldsymbol{v}_{\text{ghost}}$ is set according to the following formula:

$$\boldsymbol{v}_{\text{ghost}} = 2\boldsymbol{u}_{\text{wall}} - \boldsymbol{v}_a$$

where $\boldsymbol{u}_{\text{wall}}$ is the local wall velocity and where $\boldsymbol{v}_a$ is the fluid velocity of particle a. If the wall is fixed $\boldsymbol{u}_{\text{wall}} = \boldsymbol{0}$.

Once their velocities and densities are set, ghost particles contribute to the balance of momentum equations just like any other real fluid particle. Neither type of additional repulsive forces need to be added in order to simulate the presence of solid walls.

6. Evaluation of WC-SPH variants using Taylor–Couette flows

In this section, four WC-SPH variants are tested and compared against the pressure–velocity analytical solutions derived and presented in Section 3. All the tested variants determine the density from Eq. (40) (and then the pressure from Eq. (8)) and the viscous forces from Eq. (47). The first three variants use Eq. (46) to compute the pressure forces, while the fourth is based on the pressure equation (48). The three variants that use Eq. (46) differ in the type of Kernel used. In two of them, the classical approach of using one unique Kernel is used, variant 1 uses the Cubic Spline Kernel while variant 2 uses the Spiky Kernel. The third variant, is the one that we propose and uses a combination of both Kernels. The Spiky Kernel is used to compute the pressure force while the Cubic Spline Kernel is used for the remaining terms, including the computation of density.

In Table 1 the four tested variants are summarized.

Table 1
Summary of tested SPH variants.

Variant	Density	$\nabla \boldsymbol{v}_i$	Pressure force	Viscous force	Artif.visc. force
1	Eq. (40) Cubic	Eq. (49) Cubic	Eq. (46) Cubic	Eq. (47) Cubic	Eq. (50) Cubic
2	Eq. (40) Spiky	Eq. (49) Spiky	Eq. (46) Spiky	Eq. (47) Spiky	Eq. (50) Spiky
3	Eq. (40) Cubic	Eq. (49) Cubic	Eq. (46) Spiky	Eq. (47) Cubic	Eq. (50) Cubic
4	Eq. (40) Spiky	Eq. (49) Spiky	Eq. (48) Spiky	Eq. (47) Spiky	Eq. (50) Spiky

Note: The use of combined kernels is not new, the idea has been proposed by Muller et al. [15, 39] and has been used by others [40,24]. However, those formulations are based on SPH Laplace formulations (7) while our formulation is based on the Divergence formulation (6). Using a divergence formulation has two advantages. First, it is more general so it can be used also for non-Newtonian fluids and hyperelastic solids, and second, it leads to objective formulations when natural boundary conditions are applied (see [42]).

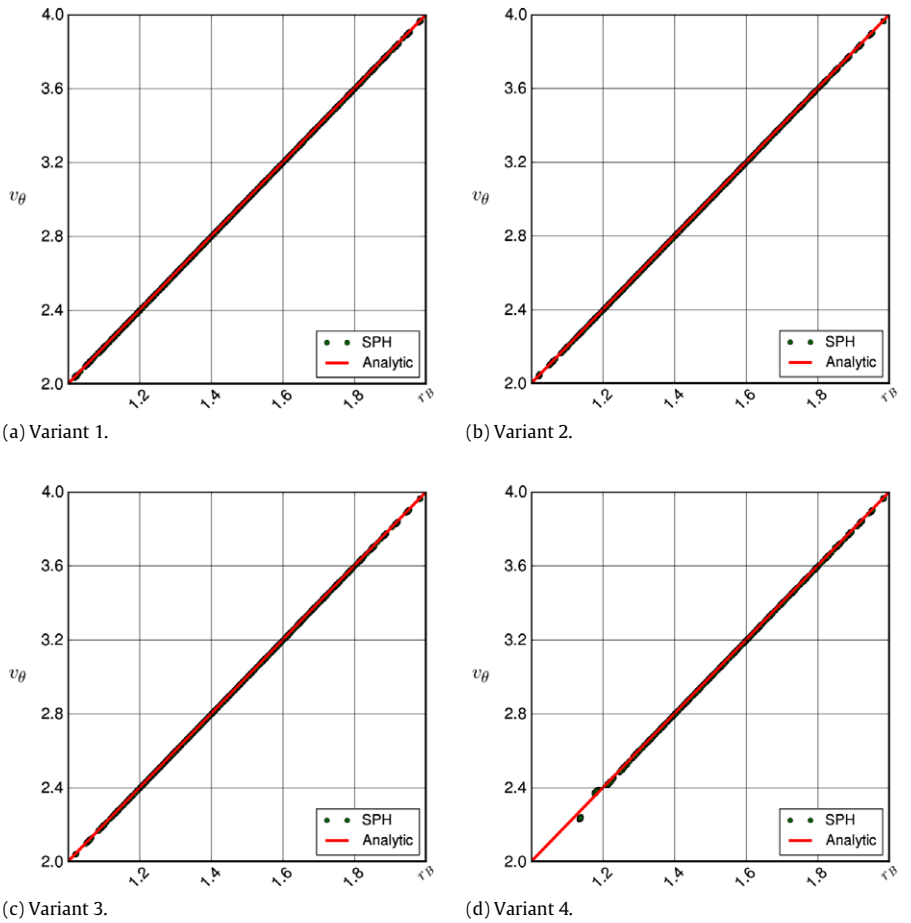

(a) Variant 1. (b) Variant 2.

(c) Variant 3. (d) Variant 4.

Fig. 7. Numerical velocity profiles obtained for the 4 SPH variants defined in Table 1 for the case of co-rotating cylinders, i.e. $\omega_A = \omega_B = 2$.

6.1. Co-rotating cylinders

Here the numerical results of the simulation corresponding to the case of co-rotating cylinders described in Section 3.3.1 are presented. SI units are used for the values of all physical quantities. For the present tests the radius of the cylinders were chosen as $r_A = 1$ and $r_B = 2$. The viscosity was $\mu = 100$, and the fluid was chosen to be a lightly compressible one ($c_s = 5, \gamma = 1$) with a water-like density $\rho_0 = 1000$. The angular rotation of both cylinders was chosen to be $\omega_A = \omega_B = \omega = 2$. The boundary conditions were simulated using ghost particles like the ones shown in Fig. 6. The tests were run using $N = 7000$ particles, each one having a mass of $m_i = 1.6$. For variants 2–4, a kernel support of $h = 0.112$ was

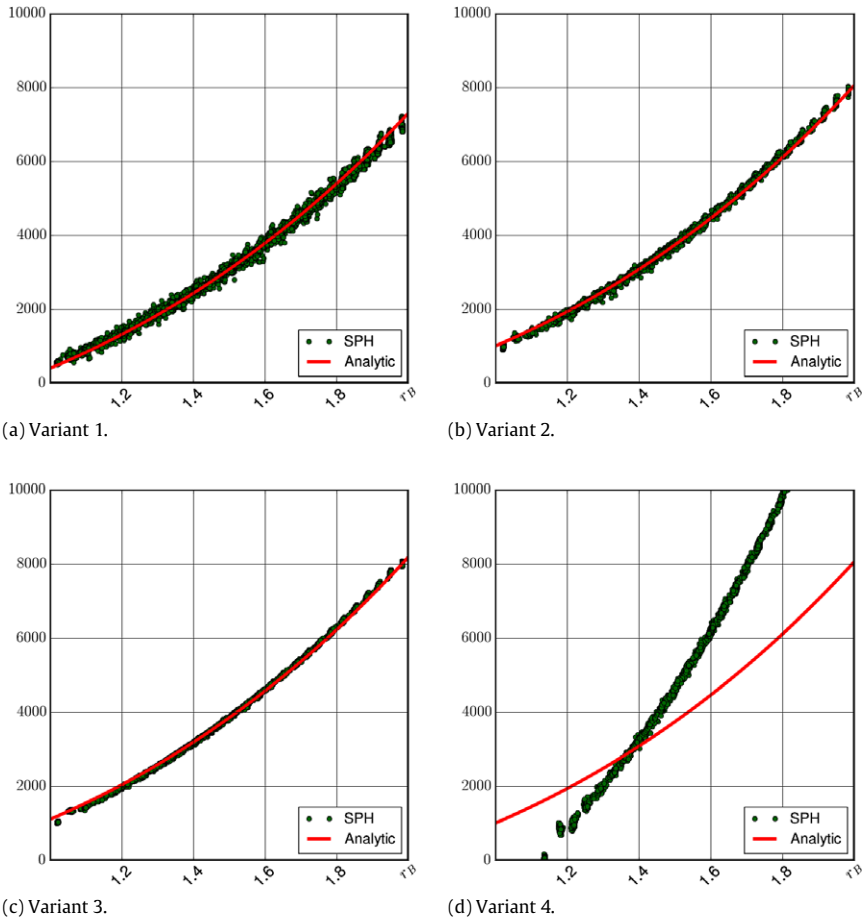

(a) Variant 1. (b) Variant 2.

(c) Variant 3. (d) Variant 4.

Fig. 8. Numerical pressure profiles obtained for the 4 SPH variants defined in Table 1 for the case of co-rotating cylinders, i.e. $\omega_A = \omega_B = 2$.

chosen corresponding to an average number of $n = 27$ neighbor particles. For variant 1, which uses the Cubic Spline Kernel to compute pressure forces, a smaller kernel support of $h = 0.08$ was chosen. Using a smaller kernel support was necessary in order to avoid the clustering problem that occurs when a kernel function with a vanishing gradient near the origin is used. This effect is well known and has been previously reported [25]. As a consequence, for variant 1, the average number of neighbor particles was $n = 15$. The obtained instantaneous numerical velocity profiles are shown in Fig. 7(a)–(d). The results show an excellent agreement between the SPH simulations and the analytical solution. Note the linear velocity profile indicating a rigid-like motion. The instantaneous numerical pressure profile formed by the particles is shown in Fig. 8(a)–(d). The results show that the three first variants match very well the theoretical pressure profile. However, as shown in Fig. 8(d), variant 4 completely fails in matching the pressure. This indicates that the SPH formulas given in Eqs. (37) and (48) (and used in Refs. [39,15,40]) lead to severely distorted results and are incorrect. On the other hand, a look at Figs. 7(c) and 8(c) shows that our proposed variant (variant 3) is the one that produces cleaner and smoother velocity and pressure profiles.

6.2. Rotating outer cylinder and fixed inner cylinder

The SPH simulations corresponding to the case described in Section 3.3.2 are presented. The same geometrical, fluid properties and SPH models of the previous subsection are chosen, but, this time the cylinders will not co-rotate, instead, the outer cylinder will be rotating with an angular velocity $\omega_B = 2$ while the inner cylinder is kept fixed $\omega_A = 0$. The obtained instantaneous numerical velocity profiles for the four SPH variants are shown in Fig. 9(a)–(d). The results also show an excellent agreement between the computed SPH velocities and the corresponding analytical solution. Note that in this case, the fluid does not acquire a rigid-like motion and the velocity profile is no longer linear. The corresponding instantaneous numerical pressure profiles formed by the particles are shown in Fig. 10(a)–(d). Like in the case of co-rotating cylinders, variant 4 gives the wrong results, proving again that approximations (37) and (48) are incorrect and should be avoided. On the other hand, in Fig. 10(a) and (b) it is shown that the classical variants 1 and 2 (in which only one type of Kernel is used in the whole SPH formulation) give particle's pressures that on average follow the analytical pressure profile. Variant 2 seems to be better than variant 1, since it gives a less noisy pressure profile and it does not suffer from particle clustering. Finally,

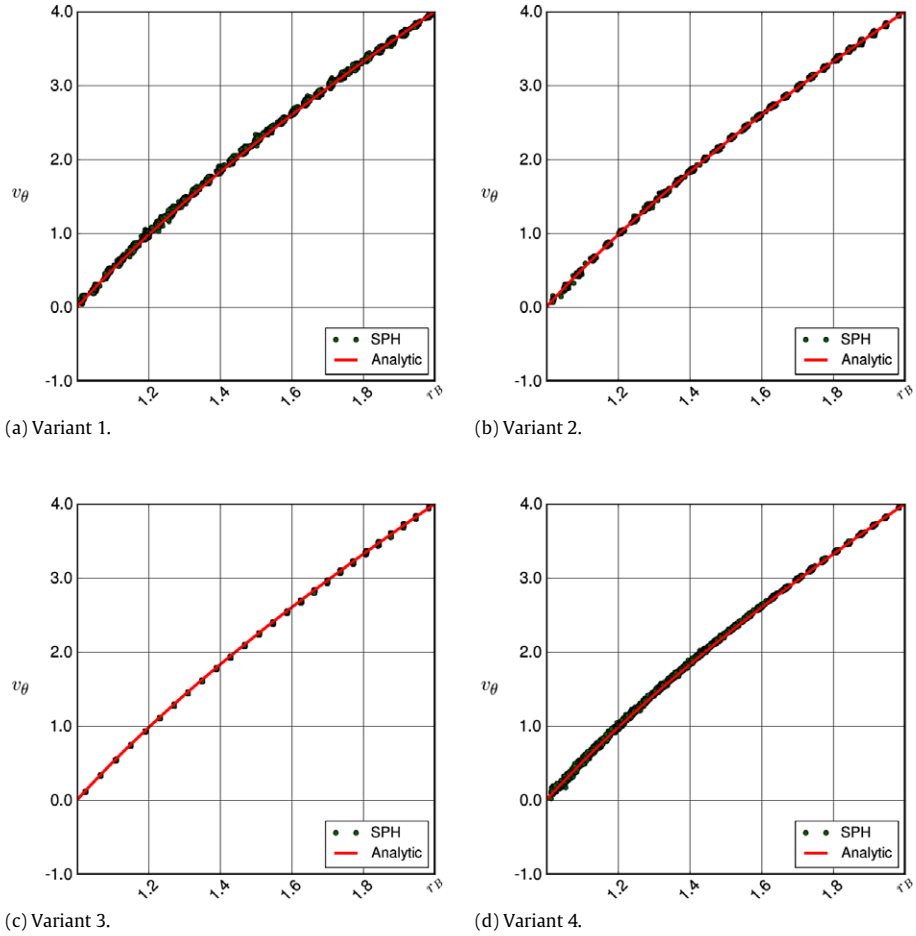

(a) Variant 1.

(b) Variant 2.

(c) Variant 3.

(d) Variant 4.

Fig. 9. Numerical velocity profiles obtained for the 4 WC-SPH variants defined in Table 1 for the case of a rotating outer cylinder $\omega_B = 2$ and a fixed inner cylinder $\omega_A = 0$.

as shown in Fig. 10(c), our proposed variant gives superior results over the other variants. The numerical pressure in the particles follows quite exactly and smoothly the theoretical pressure profile. Furthermore, like variant 2, our variant does not suffer from particle clustering.

6.3. Discussion

In all the tested variants acceptable results have been obtained for the velocity profile but not for the pressure. The pressure profile generated by variant 4 was incorrect due to the use of Eq. (48). This equation was proposed in [15] but not derived mathematically. It introduces a smoothing effect in the computation by employing an artificial factor of 2, averaging the pressure of each particle pair. This factor has no physical origin, and while it could contribute to the stability of the method, the accuracy suffers considerably. On the contrary, the Eq. (46) can be derived mathematically, and does not introduce non-physical constants, which is the reason the authors consider the variant 4 is only suitable for physical based animations, but not for engineering problems.

If only variants 1–3 are considered, it can be seen that variant 3 performs better. It uses the Spline kernel for the density and the Spiky for the pressure. Although it might seem more reasonable to use the same kernel for all the fields, it is not mandatory in SPH as long as the kernels satisfy the conditions given in [12]. The observed experimental advantages of using different kernels can be explained by examining the fields approximated. The density is very noisy in WC-SPH, so it is better to use a Gaussian-like kernel as the spline because it has good smoothing properties which reduce density and pressure oscillations. For the pressure force, the kernel gradients must be observed. As it can be seen in Fig. 11 the Spline gradient tends to 0 as it approaches the origin, this leads to a pressure force that vanishes or is too small when the particles are very near, contrary to the expected physical behavior. This does not happen with the Spiky kernel that has a peak at its origin generating strong repulsive forces. The Spiky is also very similar to a delta function, this shape has a smaller smoothing effect than the Spline letting the particles move more freely and preserves the local pressure differences better.

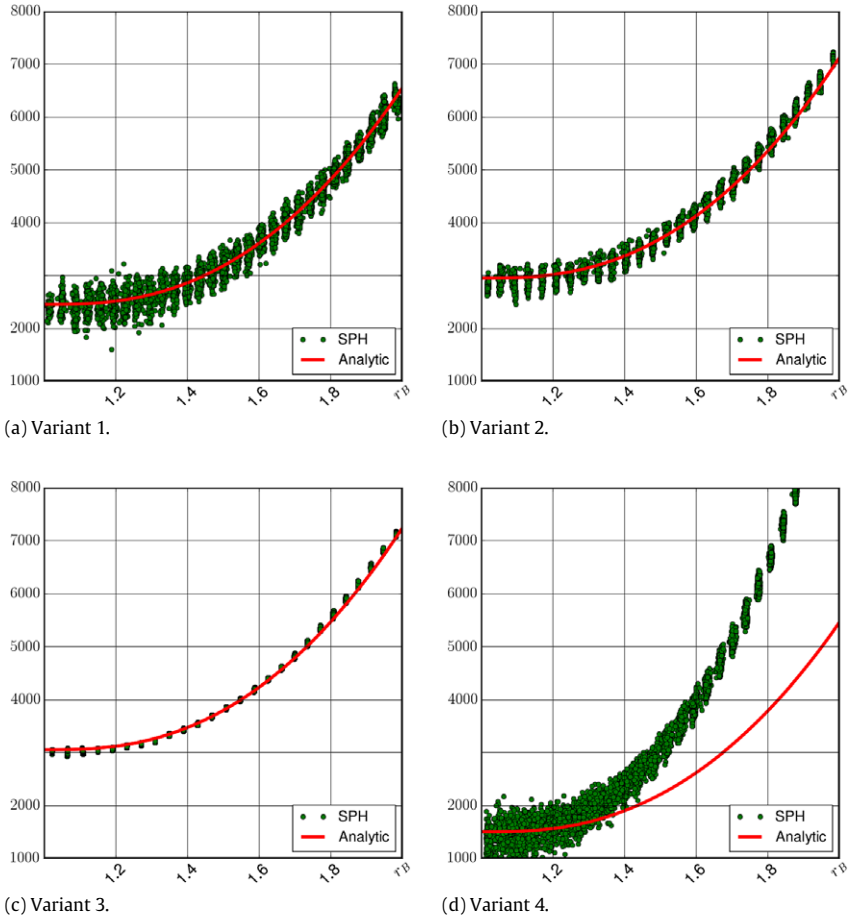

(a) Variant 1. (b) Variant 2.

(c) Variant 3. (d) Variant 4.

Fig. 10. Numerical pressure profiles obtained for the 4 WC-SPH variants defined in Table 1 for the case of a rotating outer cylinder $\omega_B = 2$ and a fixed inner cylinder $\omega_A = 0$.

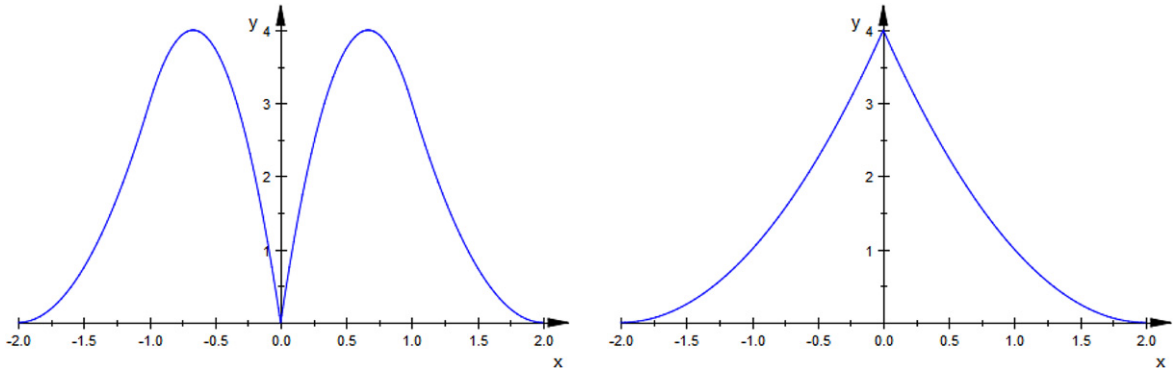

(a) Cubic spline. (b) Spiky.

Fig. 11. SPH kernels gradients.

7. Conclusions

In the first portion of this article, analytical solutions of the Navier–Stokes equations have been derived for the case of planar Taylor–Couette flows. The analytical solutions provide pressure–velocity profiles for both compressible and weakly-compressible fluids governed by the same equations of state that are commonly used in WC-SPH. In the second part of the paper, the obtained theoretical solutions have been employed to evaluate a WC-SPH variant based on the divergence form of the Navier–Stokes equations and on the simultaneous use of two different kernels. As shown in the numerical tests,

the proposed variant gives better, smoother solutions than other traditional variants. This is particularly noticeable in the pressure solutions. Finally, it must be pointed out that the derived analytical solutions can be used as a set of flow benchmark tests to validate numerical formulations either of the SPH type or of any other type.

References

[1] L.B. Lucy, Numerical approach to testing the fission hypothesis, The Astronomical Journal 82 (1977) 1013–1024.
[2] R.A. Gingold, J.J. Monaghan, Smoothed particle hydrodynamics: theory and application to non-spherical stars, Monthly Notices of the Royal Astronomical Society 181 (1977) 375–389.
[3] J. Monaghan, Smoothed particle hydrodynamics, Annual Review of Astronomy and Astrophysics 30 (1992) 543–574.
[4] A.R. Frederic, C.L. James, Smoothed particle hydrodynamics calculations of stellar interactions, Journal of Computational and Applied Mathematics 109 (1999) 213–230.
[5] J.J. Monaghan, J.C. Lattanzio, A simulation of the collapse and fragmentation of cooling molecular clouds, The Astrophysical Journal 375 (1991) 177–189.
[6] P. Berczik, Modeling the star formation in galaxies using the chemodynamical SPH code, Astronomy and Astrophysics 360 (2000) 76–84.
[7] W.H. Lee, Newtonian hydrodynamics of the coalescence of black holes with neutron stars III, irrotational binaries with a stiff equation of state, Monthly Notices of the Royal Astronomical Society 318 (2000) 606–624.
[8] J.J. Monaghan, Modeling the universe, Proceedings of the Astronomical Society of Australia (ISSN: 0066-9997) 8 (3) (1990) 233–237.
[9] K.P. Thiagarajan, A. Rafiee, An SPH projection method for simulating fluid-hypoelastic structure interaction, Computer Methods in Applied Mechanics and Engineering 198 (2009) 2785–2795.
[10] B. Solenthaler, J. Schlfli, R. Pajarola, A unified particle model for fluid–solid interactions, Computer Animation and Virtual Worlds 18 (2007) 67–82.
[11] J. Schlafli, Simulation of fluid–solid interaction, Ph.D. Thesis, VMML. University of Zurich, 2005.
[12] M. Liu, G. Liu, Smoothed Particle Hydrodynamics: A Meshfree Particle Method, World Scientific Publishing Co. Pvt. Ltd., 2003.
[13] S. Idelsohn, J. Marti, A. Limache, E. Onate, A unified Lagrangian formulation for elastic solids and incompressible fluids. application to fluid–structure interaction problems via the PFEM, Computer Methods in Applied Mechanics and Engineering 197 (2008) 1762–1776.
[14] S. Idelsohn, E. Onate, F. Del-Pin, The particle finite element method a powerful tool to solve incompressible flows with free-surfaces and breaking waves, International Journal for Numerical Methods in Engineering 61 (2004) 964–989.
[15] D. Charypar, M. Müller, M. Gross, Particle-based fluid simulation for interactive applications, in: M. Lin, D. Breen (Eds.), SIGGRAPH Symposium on Computer Animation, pp. 154–159.
[16] T. Harada, S. Koshizuka, Y. Kawaguchi, Real-time fluid simulation coupled with cloth, Theory and Practice of Computer Graphics (2007).
[17] F. Losasso, J.N. Kwatra, R. Fedkiw, Two-way coupled SPH and particle level set fluid simulation, IEEE Transactions on Visualization and Computer Graphics 14 (2008) 797–804.
[18] J. Monaghan, Smoothed particle hydrodynamics, Reports on Progress in Physics 68 (2005) 1703–1759.
[19] J. Patrick, Y. Zhu, J. Morris, Modeling low Reynolds number incompressible flows using SPH, Journal of Computational Physics 136 (1997) 214–226.
[20] R. Rook, A. Suleman, M. Yildiz, SPH with the multiple boundary tangent method, International Journal for Numerical Methods in Engineering (2008).
[21] S.J. Cumins, M. Rudman, An SPH projection method, Journal of Computational Physics 152 (1999) 584–607.
[22] S. Koshizuka, Y. Oka, H. Tamako, A particle method for calculating splashing of incompressible viscous fluid, in: Int. Conf. Math. Comput., vol. 2, 1995, pp. 1514–1521.
[23] S. Koshizuka, A. Nobe, Y. Oka, Numerical analysis of breaking waves using the moving particle semi-implicit method, International Journal for Numerical Methods in Fluids 26 (1998) 751–769.
[24] M. Vesterlund, Simulation and rendering of a viscous fluid using smoothed particle hydrodynamic, Ph.D. Thesis, VRLab, Umea University, 2004.
[25] M. Desbrun, M. Cani, Smoothed particles: a new paradigm for animating highly deformable bodies, in: Proceedings of Eurographics Workshop on Computer Animation and Simulation, EGCAS'96, 1996, pp. 61–76.
[26] P.W. Cleary, Modelling confined multi-material heat and mass flows using SPH, Applied Mathematical Modelling 22 (1998) 981–993.
[27] P.W. Cleary, New implementation of viscosity: tests with Couette flows, Technical Report, SPH Technical Note #8, CSIRO Division of Mathematics and Statistics, 1996.
[28] P.W. Cleary, Modelling confined multi-material heat and mass flows using SPH, in: Inter. Conf. on CFD in Mineral & Metal Processing and Power Generation CSIRO, pp. 1–23.
[29] E.-S. Lee, C. Moulinec, R. Xu, D. Violeau, D. Laurence, P. Stansby, Comparisons of weakly compressible and truly incompressible algorithms for the SPH mesh free particle method, Journal of Computational Physics 227 (2008) 8417–8436.
[30] R. Xu, P. Stansby, D. Laurence, Accuracy and stability in incompressible SPH (ISPH) based on the projection method and a new approach, Journal of Computational Physics 228 (2009) 6703–6725.
[31] M. Safdari-Shadloo, A. Zainali, S. Sadek, M. Yildiz, Improved incompressible smoothed particle hydrodynamics method for simulating flow around bluff bodies, Computer Methods in Applied Mechanics and Engineering 200 (2011) 1008–1020.
[32] G. Shobeyri, L. Farhadi, B. Ataie-Ashtiani, Modified incompressible SPH method for simulating free surface problems, Fluid Dynamics Research 40 (2007) 637–661.
[33] R. Fatehi, M.T. Manzari, A consistent and fast weakly compressible smoothed particle hydrodynamics with a new wall boundary condition, International Journal for Numerical Methods in Fluids 68 (2011) 905–921.
[34] D. Molteni, A. Colagrossi, A simple procedure to improve the pressure evaluation in hydrodynamic context using the SPH, Computer Physics Communications 180 (2009) 861–872.
[35] C. Antoci, M. Gallati, S. Sibilla, Numerical simulation of fluid–structure interaction by SPH, Computers and Structures 85 (2007) 879–890.
[36] A. Limache, P. Sanchez, L. Dalcin, S. Idelsohn, Objectivity tests for Navier–Stokes simulations: the revealing of non-physical solutions produced by laplace formulations, Computer Methods in Applied Mechanics and Engineering 197 (2008) 4180–4192.
[37] R. Egli, F. Lin, F. Colin, Smoothed Particle Hydrodynamics: A Meshfree Particle Method, World Scientific Publishing Co. Pvt. Ltd., 2003.
[38] I.J. Schoenberg, Contributions to the problem of approximation of equidistant data by analytic functions, Quarterly of Applied Mathematics 4 (1946) 45–49.
[39] M. Müller, S. Schirm, M. Teschner, Interactive blood simulation for virtual surgery based on smoothed particle hydrodynamics, Technology and Health Care 12 (2004) 25–51.
[40] T. Harada, S. Koshizuka, Y. Kawaguchi, Smoothed particle hydrodynamics on GPUS, in: Proc. of Computer Graphics International, pp. 63–70.
[41] A. Colagrossi, M. Landrini, Numerical simulation of interfacial flows by smoothed particle hydrodynamics, Journal of Computational Physics 191 (2003) 448–475.
[42] A. Limache, S. Idelsohn, R. Rossi, E. Onate, The violation of objectivity in laplace formulations of the Navier–Stokes equations, International Journal for Numerical Methods in Fluids 54 (2007) 639–664.